nature physics

LETTERS

https://doi.org/10.1038/s41567-018-0161-5

Corrected: Publisher Correction

Long-distance spin transport through a graphene quantum Hall antiferromagnet

Petr Stepanov[1,2,7], Shi Che[1,2,7], Dmitry Shcherbakov[1,2], Jiawei Yang[1,2], Ruoyu Chen[2], Kevin Thilahar[1], Greyson Voigt[1], Marc W. Bockrath[1,2], Dmitry Smirnov[3], Kenji Watanabe[4], Takashi Taniguchi[4], Roger K. Lake[5*], Yafis Barlas[1,5*], Allan H. MacDonald[6*] and Chun Ning Lau[1,2*]

Because of their ultrafast intrinsic dynamics and robustness against stray fields, antiferromagnetic insulators[1–3] are promising candidates for spintronic components. Therefore, long-distance, low-dissipation spin transport and electrical manipulation of antiferromagnetic order are key research goals in antiferromagnetic spintronics. Here, we report experimental evidence of robust spin transport through an antiferromagnetic insulator, in our case the gate-controlled state that appears in charge-neutral graphene in a magnetic field[4–6]. Utilizing quantum Hall edge states as spin-dependent injectors and detectors, we observe large, non-local electrical signals across charge-neutral channels that are up to 5 μm long. The dependence of the signal on magnetic field, temperature and filling factor is consistent with spin superfluidity[1,2,4,7–10] as the spin-transport mechanism. This work demonstrates the utility of graphene in the quantum Hall regime as a powerful model system for fundamental studies in antiferromagnetic spintronics.

Spin currents in magnetic insulators can be carried with dissipation by magnon quasiparticles[11,12], or collectively and without dissipation by spin supercurrents in systems with easy-plane magnetic order[1,2,4,7–10]. Whereas magnon transport is less efficient in an ideal antiferromagnetic insulator (AFMI) than in a ferromagnetic insulator, superfluidity is theoretically possible in both cases. Although the potential of antiferromagnetic materials[1–3] as electrically tunable active spintronic components has been recognized[13], and important progress has been made[3,14–17], spin transport through an AFMI thicker than ~10 nm has yet to be demonstrated.

In a parallel thread of scientific progress, monolayer graphene has emerged as a versatile platform to investigate ordered states of matter. In strong magnetic fields, the approximate SU(4) spin-valley invariance symmetry is frequently broken, giving rise to gate tunable order[5,6,18–30]. For example, whereas states at Landau level filling factor $\nu=\pm2$ do not have broken symmetries and support two co-propagating chiral edge channels with opposite spins, states at $\nu=\pm1$ are spontaneously spin-polarized and support a single spin-polarized chiral edge channel. The $\nu=0$ state of charge-neutral graphene, which has no counterpart in traditional GaAs-based quantum Hall systems, is particularly interesting: it is a true insulator with no edge states and diverging longitudinal resistance. The consensus emerging from experiment is that the $\nu=0$ state is an AFMI, with nearly opposite easy-plane spin polarizations on the two sublattices of the graphene lattice[5,6]; the spins are very slightly canted out-of-plane due to Zeeman coupling. However, a direct demonstration of the antiferromagnetic order has been missing prior to the present work.

Because of its gate-tunable magnetic order and extremely weak spin–orbit coupling, high-quality graphene in the quantum Hall regime has been proposed as an attractive model system for fundamental spintronics studies[4,31]. In this paper, we implement a previous proposal[4], by using the $\nu=0$ state of graphene as the AFMI and combining the $\nu=\pm2$ and ±1 states to realize spin injectors and detectors. We detect a large non-local voltage signal, up to 225 μV, that is transmitted up to 5 μm across the AFMI. The signal disappears when the filter regions are tuned away from the $\nu=\pm1$ state that supplies a spin-dependence. Both the magnitude of the non-local signal and the transport distances are orders of magnitudes larger than in oxide-based AFMIs[3,14–17], suggesting that a fundamentally different mechanism is at play.

The operating principle and geometry of the device, which consists of a graphene sheet in the *xy* plane with a series of separately contacted top gates, is illustrated in Fig. 1a–c (ref. [4]). The central top gate V_{ctg} is used to tune the graphene region underneath to $\nu=0$, at which the ground state is an AFMI[5,6,18–29]. Zeeman coupling to the antiferromagnetic order leads to A and B sublattice spins that are nearly in the *xy* plane, but with a slight canting towards the field direction. The canting angle θ depends on the ratio of the Zeeman energy to the valley-flip isospin anisotropy energy[5,6]. To the left and right of the antiferromagnetic state are the injection and detector regions, respectively, each consisting of a top-gated region flanked by two 'bare' (non-top-gated) regions. During device operation, the filling factors of the left (right) top-gated regions are tuned to $\nu_{inj}=-1$ ($\nu_{det}=-1$) at which the ground state is a ferromagnetic quantum Hall insulator with a conducting chiral edge channel that is fully spin-polarized opposite to the net magnetization direction, and the bare regions are tuned to $\nu=-2$, which has a non-magnetic quantum Hall ground state that supports chiral edge channels of both spins. (For illustration, the device here is hole-doped so that $\nu=-2$ and -1 states are employed; similar behaviour occurs for $\nu=+2$ and $+1$ in the electron-doped regime.) In the injection region, a voltage bias V_{bias} is applied between the two 'bare' regions so as to establish a chemical potential difference between the transmitted ↑ and reflected ↓ spin channels. When impinging on the antiferromagnetic region, the incident spin current at the left antiferromagnetic interface can produce a spin-transfer torque that favours the formation of spiral (Néel) spin textures that carry spin current

[1]Department of Physics and Astronomy, University of California, Riverside, CA, USA. [2]Department of Physics, Ohio State University, Columbus, OH, USA. [3]National High Magnetic Field Laboratory, Tallahassee, FL, USA. [4]National Institute for Materials Science, Tsukuba, Japan. [5]Department of Electrical and Computer Engineering, University of California, Riverside, CA, USA. [6]Department of Physics, University of Texas at Austin, Austin, TX, USA. [7]These authors contributed equally: Petr Stepanov, Shi Che. *e-mail: rlake@ece.ucr.edu; yafisb@ucr.com; macd@physics.utexas.edu; lau.232@osu.edu

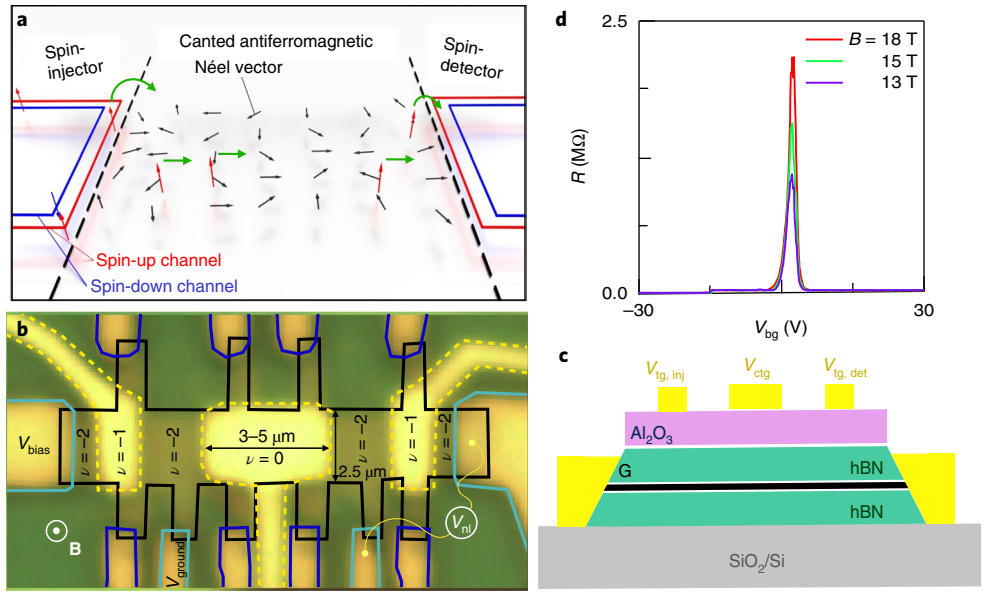

Fig. 1 | Device geometry, operating principle and characterization. a, Schematics of spin transport through the ν=0 AFM state in graphene. The black, red and green arrows indicate Néel vectors of the AFM, polarization of transported spin, and direction of spin transport, respectively. **b**, Optical image of Device 1. The edges of the graphene Hall bar, metal gates, and metal contacts have been outlined to aid visualization. Dimensions and biasing are shown. **c**, Side-view schematic of device geometry. **d**, $R_{xx}(V_{bg})$ from Device 1 at the charge neutrality point for B=13 T, 15 T and 18 T, respectively. Note that the resistance more than doubles when B increases from 13 to 18 T.

collectively[4,7,8,32]. In the detector region, this spin current is converted into a spin-polarized charge current via a reciprocal process and measured as a non-local voltage V_{nl} between the two voltage probes attached to the two $\nu=-2$ regions.

Because the magnetic states of graphene in the quantum Hall regime are susceptible to disorder[18], realization of this proposal requires fabrication of devices of exceptional quality[33]. With this goal, we have assembled long monolayers encapsulated in hexagonal boron nitride (hBN) sheets with three independent top gates (Fig. 1b,c). The charge densities of the four bare regions are controlled by the back-gate voltage V_{bg}, while those of the top-gated regions are tuned by both back and top gates. At low temperature T=0.3 K, the longitudinal resistivity of the insulating $\nu=0$ state increases with magnetic field, indicating the establishment of a robust AFMI state[5,24,25] (Fig. 1d).

Here we present data from two different devices. The length L and width W of the central top gate, the antiferromagnetic region during device operation, are ~5 μm (3 μm) and 2.5 μm (1.9 μm), respectively, for Device 1 (Device 2). Our main experimental findings, taken from Device 1, are presented in Fig. 2a–c. We first explore spin transport by independently modulating the filling factors ν_{inj} and ν_{det} of the top-gated injector and detector regions, while conserving $\nu=0$ and $\nu=-2$ states at the central top-gated and the bare regions, respectively. We apply a bias voltage V_{bias}=0.4 V while monitoring the non-local signal V_{nl} (see device configuration in Fig. 2d). Figure 2a plots V_{nl} (colour) at B=18 T as ν_{inj} and ν_{det} vary from −3 to +1. Prominent signals are observed only when both ν_{inj} and ν_{det} are tuned to be close to $\nu=-1$ (that is, only when the detecting and injecting regions contain spin-filters). The dark blue area for $\nu_{det}>-0.5$ signifies amplifier saturation when the right top-gated region enters the insulating AFM state. Figure 2b,c shows the individual line traces of V_{nl} for fixed $\nu_{inj}=-1$ and fixed $\nu_{det}=-1$, respectively. The non-local signal detected across the 5 μm channel is exceedingly large, with a maximum amplitude of ~225 μV centered at $\nu_{inj}=\nu_{det}=-1$. (We attribute the fluctuations in Fig. 2b, which are not reproduced in repeated measurements, to amplifier offset drift and 1/f noise.)

Similar data are observed in two other samples. Figure 2e,f presents similar $V_{nl}(\nu_{inj}, \nu_{det})$ data from Device 2, which has high electron mobility and an exceedingly robust $\nu=1$ state. At V_{bias}=0.065 V, a prominent non-local signal ~140 μV is observed only around $\nu_{inj}=\nu_{det}=1$, thus demonstrating a similar spin-selective response in the electron-doped regime. Additional data are presented in the Supplementary Information.

We note that the bias voltages (V_{bias}, ~10 mV to 0.4 V) employed in this study are comparable to or in excess of the Landau level gaps of the relevant quantum Hall states in graphene. However, we can exclude simple hot-electron or heating effects as the source of our non-local signal because it is spin-selective. We also exclude quantum Hall breakdown since it is controlled mainly by the electric field across the sample; the breakdown electric field is estimated to be ~26 mV nm^{-1} at B=18 T, three orders of magnitude larger than that induced by our largest bias, ~0.1 mV nm^{-1} (see Supplementary Information for a more detailed discussion).

A number of different physical mechanisms could be responsible for the non-local signal: charge tunnelling, percolation, drift or diffusion, a spin Seebeck effect carried by thermal magnons, or spin superfluidity in the easy-plane AFMI $\nu=0$ channel. In the remainder of the paper, we present data that either support or undermine these different scenarios. We find that the spin-superfluidity mechanism is most consistent with the data. If the non-local signal were due to charge transport, either via tunnelling, percolation, drift or diffusion, one would expect that that V_{nl} would increase as the channel conductivity increases, since the charge could then more easily traverse the channel. When the magnetic field is reduced from 18 T to 15 T, the conductivity of the $\nu=0$ channel increases by a factor of 1.4 (Fig. 1d). However, V_{nl} decreases by a factor of 2.8 to ~80 μV (yellow line trace, Fig. 2b). The decrease in V_{nl} as the $\nu=0$ state becomes more conductive contradicts the trend expected from a charge leakage mechanism. It also rules out transport by percolation of compressible/incompressible stripes that are estimated to be ~10–20 nm wide[34]. The observation is, however, consistent with a spin-transport mechanism, which should be enhanced by the presence of a more robust AFMI state.

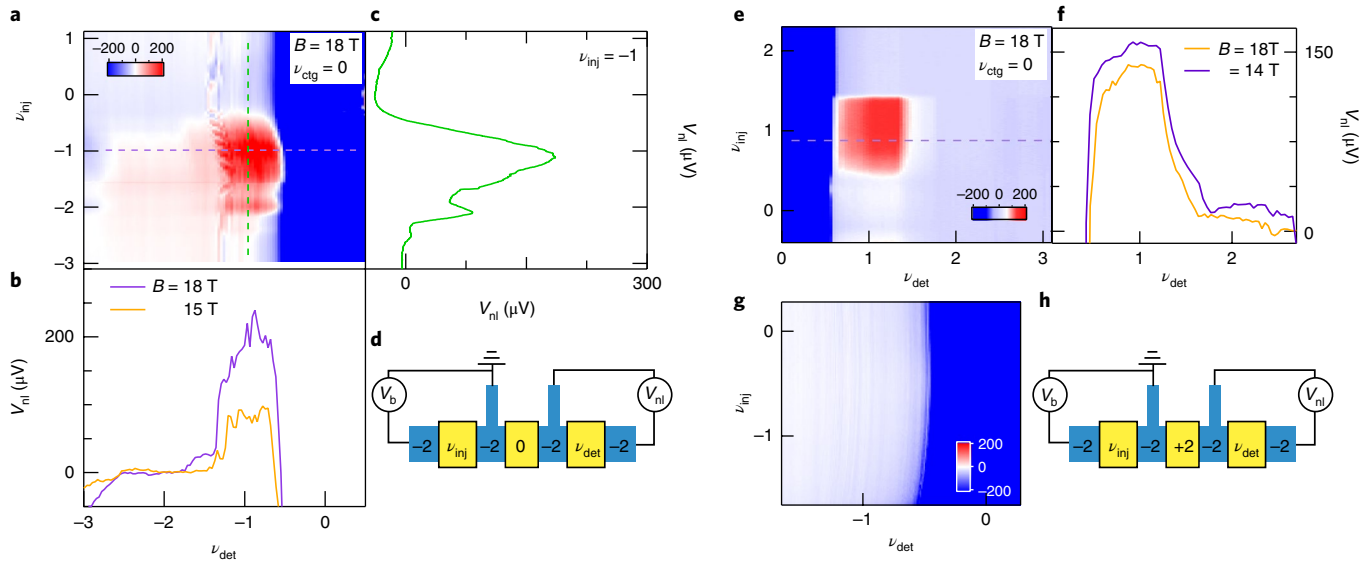

Fig. 2 | Non-local transport data at *T*=260 mK. a–d, $V_{nl}(\nu_{inj}, \nu_{det})$ from Device 1 at V_{bias}=0.4 V and B=18 T (**a**) using the device configuration shown in **d**, and line traces $V_{nl}(\nu_{det})$ at ν_{inj}=−1 (**b**) and $V_{nl}(\nu_{inj})$ at ν_{det}=−1 (**c**). The yellow curve in **b** is taken at B=15 T. The line traces are offset by 30 μV to account for amplifier offset. **e**,**f**. Similar data from Device 2 at V_{bias}=0.065 V. **g**,**h**. $V_{nl}(\nu_{inj}, \nu_{det})$ from Device 1 at B=18 T (**g**) when the central top-gated region is set to ν=2, using the device configuration shown in **h**.

To further confirm that the non-local signal arises from transport of a pure spin current through the antiferromagnet, we perform a control study in which the central region is tuned instead to the insulating $\nu=+2$ state, which has unpolarized chiral edge channels (Fig. 2h). The $V_{nl}(\nu_{inj}, \nu_{det})$ map at $B=18$ T (Fig. 2g) for this case indicates minimal response. Thus, the non-local signal is small when any one of the three regions (the injector, the detector, or the centre region) is tuned to a $\nu=-2$ or $\nu=+2$ state. Taken together, these control measurements demonstrate that non-local signals indeed arise from spin transport, and not drift, diffusion, or percolation of charge currents (see Supplementary Information for additional analysis).

We note that non-local signals at the Dirac point in graphene have been observed previously[35], but differ dramatically in origin from those in the current work. In ref. [35], the entire device is gated into the $\nu=0$ state, and the non-local signals, which persisted at high temperature and low magnetic fields, were attributed to long-range flavour Hall effects, although they could also arise from magneto-thermoelectric effects[36]. In contrast, our devices are specifically configured with the $\nu=\pm2/\pm1/\pm2$ regions for spin injection and detection, and the non-local signal appears only in the low-temperature, high-magnetic-field regime where the AFMI state forms. Moreover, our control measurements rule out spin and valley Hall effects.

We have also examined the dependence of the non-local signal on the bias voltage V_{bias} that controls the electro-chemical potential difference between the up and down spins in the injector. Using Device 1, we varied the left and right top gate voltages so that $\nu_{inj}=\nu_{det}$ throughout the measurements, while maintaining the 'bare' regions at $\nu=-2$ and the central top-gated region at $\nu=0$. Figure 3a presents V_{nl} versus V_{bias} and the filling factors of the injector and detector regions. As before, prominent signals are observed for $\nu_{inj}=\nu_{det}=-1$. For $V_{bias}>0$, the signal is approximately linear in V_{bias} (Fig. 3b). The smallest value of V_{bias} at which non-local signal is detectable is < ~0.01 V and limited by resolution of the sweep. This small V_{bias} value, together with the linear dependence, confirms that Joule heating is not the origin of our signal. On the other hand, since the non-local voltage is expected to be linear in V_{bias} for both spin-superfluid and charge-current mechanisms[4], this observation does not, on its own, rule out either mechanism.

Finally, we compare the temperature dependence of the non-local signal of Device 1 with that of the quantum Hall effects. At $B=18$ T, the magnitude of the non-local signal decreases with increasing T, and disappears at ~45 K. Since spin transport in our devices depends critically on the quantum Hall states in graphene, we also measure $R_{xx}(V_{bg})$ at $B=18$ T and temperatures ranging from 2.7 K to 85 K. As illustrated in Fig. 3c, the $\nu=0$ and $\nu=-2$ states are very robust and remain well quantized even at $T=85$ K. The $\nu=-1$ state is more fragile; its R_{xx} increases with T and the quantum Hall effect is barely resolved when T increases to ~35 K. To compare the dependences of the quantum Hall states and the non-local signal, in Fig. 3d we plot R_{xx} (right axis, blue triangles) and V_{nl} (left axis, red squares) versus $1/T$ in Arrhenius scales. Both data sets can be satisfactorily fitted to a thermal activation model, with characteristic temperatures of 23.8±2.2 K and 24.8±2.4 K, respectively. The similar T-dependences strongly suggest that the non-local transport signals in the range of 2 to 40 K are dependent on the spin-filtering action of the $\nu=-1$ state, which enables both spin injection and detection. At the same time, the temperature dependence of V_{nl} is opposite to that expected from a spin Seebeck effect mediated by thermal magnons.

We now further consider the two-pin transport mechanisms mediated by magnetic order.

Spins can be carried either by magnon quasiparticles or collectively in the form of spin supercurrents. In an ideal antiferromagnet, magnons do not carry spin. However, the magnetic order of the $\nu=0$ quantum Hall state is slightly canted in the z direction, so the z-injected spin current could drive magnons that diffuse across the AFMI, transporting spins from one end to the other. The spin carried by a magnon is proportional to the small[5] canting angle θ, which is proportional to the ratio of the Zeeman energy to the valley-flip anisotropy energy and estimated to be is ~0.04. Thus, canting-induced magnon transport of spin across the few-micrometre-long AFMI should be weak. Also, as noted above, the monotonic decline of the non-local signals with increasing temperature is opposite to that expected from magnon-mediated transport, since magnons are thermally activated and should be more effective at higher temperatures. This T-dependence, together with the linear dependence of the non-local signal down to relatively small biases,

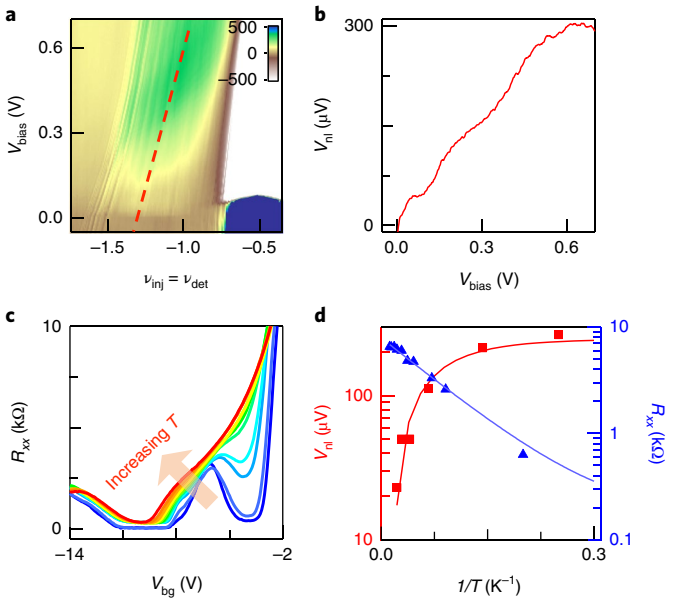

Fig. 3 | Bias and temperature dependence of non-local signal from Device 1. a, $V_{nl}(V_{bias}, \nu_{det})$ data at B=18 T. **b**, A line cut $V_{nl}(V_{bias})$ along the dotted line shown in **a**. **c**, $R_{xx}(V_{bg})$ at B=18 T with T=2.7, 5, 11, 14, 22, 27, 35, 45, 55, 70 and 84 K (bottom to top). **d**. Maximum non-local signal at $\nu_{inj}=\nu_{det}=-1$ (left axis) and $R_{xx}(T)$ of the $\nu=-1$ state (right axis) plotted versus $1/T$ on an Arrhenius scale. The solid lines are fits to a thermal activation model.

also suggests that heating is not significant in the system, since otherwise the signal should be independent of temperature until the substrate temperature exceeds that induced by the bias.

Because of the above considerations, and a spin-transport distance that is 10^3–10^4 times longer than previous studies of magnons in oxide-based AFMIs[3,14–17], we conclude that a fundamentally different mechanism underlies our experimental results. Thus, we consider the only other known spin-transport mechanism in an AFMI—coherent Néel textures that allow superfluid transport of spins polarized in the z-direction (see Supplementary Movie for an animation of superfluid spin transport). In the limit of large spin stiffness, efficient spin-injection, and weak violation of valley-projected number conservation, the non-local voltage is expected[37] to satisfy

$$\frac{V_{nl}}{V_{bias}} = \frac{F_{inj} g_{inj}}{F_{inj} g_{inj} + \alpha \frac{e^2}{h} \frac{A}{2\pi l_B^2}} \quad (1)$$

(The easy-plane ferromagnet case considered in ref. [37] and the easy-plane antiferromagnet case relevant here have identical spin-superfluid responses to injected spin-currents.) Here g_{inj} is the longitudinal conductance of the $\nu=\pm1$ regions, which is expected to be very close to e^2/h (where e is the electronic charge and h is the Planck constant), l_B is the magnetic length, F_{inj} is the efficiency factor for spin-injection, A is the area of the antiferromagnetic region, and α is the magnetization damping parameter. To estimate F_{inj}, it is important to consider how charge is carried along the perimeter of the $\nu=\pm2$ regions, which are surrounded on three sides by $\nu=0$ regions that support two hole-like chiral edge channels. For boundaries between $\nu=-2$ and vacuum these channels have spins polarized along and opposite to the magnetic field. However, for the critical boundary between the $\nu=\pm2$ region and the $\nu=0$ antiferromagnet, the edge channels in the narrow boundary limit will be those of the occupied quasiparticle states from the broken symmetry $N=0$ Landau level which have spin-polarization close to the xy plane. Because these quasiparticles cannot carry z-polarized spins, F_{inj} can be close to 1 if the boundary can be made sharp. Since, in our experiments $V_{nl}/V_{bias}\sim10^{-4}$ (10^{-3}) and the antiferromagnetic area A=12.5 μm^2 (6.6 μm^2) for Device 1 (Device 2), we obtain from equation (1) that $\alpha \sim 10^{-2}\ F_{inj}$, consistent with α values in the 10^{-4} to 10^{-2} range typical of AFMIs[38–40]. Magnetization damping in the $\nu=0$ antiferromagnetic state is probably due to decay channels opened up by density inhomogeneities within the sample[41].

The applied voltage, gate voltage, magnetic field and temperature dependencies of the non-local voltage are all consistent with the mechanism of superfluid spin transport across a 3–5-μm AFMI state. Other possible interpretations (charge leakage, spin Seebeck, Zeeman spin and valley Hall effects) of our observations are contradicted by one or more trends of the data. The negative signal at $\nu_{det}=-3$ from Device 1 (Fig. 2a,b) is also intriguing, as it suggests similar spin polarization for the higher Landau levels[28,42] that may also be similarly used as spin filters. Taken together, we therefore tentatively attribute the observed robust non-local signal across the 5-μm AFMI state in graphene to collective spin transport.

In a related recent preprint on long-distance spin manipulation and transport using an all-graphene electrical circuit in the quantum Hall regime, Wei et al.[43] have reported the observation of magnon transport through the ferromagnetic insulating bulk of the $\nu=1$ state. This and our work further establish graphene in the quantum Hall regime as a model system for fundamental studies of antiferromagnetic and ferromagnetic spintronics. Our results for $\nu=0$ spin transport call for further work to refine the $\nu=\pm1$ spin filters, to establish the length, width and mobility dependence of the spin transport signals, to quantify the role of valley-dependent interactions in the AFMI, and to understand the junctions between $\nu=\pm2$/vacuum and $\nu=\pm2$/AFMI interfaces. The long-term goal of this research is to achieve nearly dissipationless spin-transport in practical magnetic materials for information processing and storage applications.

Methods

Methods, including statements of data availability and any associated accession codes and references, are available at https://doi.org/10.1038/s41567-018-0161-5.

Received: 17 November 2017; Accepted: 2 May 2018;
Published online: 11 June 2018

References

1. Baltz, V. et al. Antiferromagnetism: the next flagship magnetic order for spintronics? *Rev. Mod. Phys.* **90**, 015005 (2018).
2. Jungwirth, T., Marti, X., Wadley, P. & Wunderlich, J. Antiferromagnetic spintronics. *Nat. Nanotech.* **11**, 231–241 (2016).
3. Wadley, P. et al. Electrical switching of an antiferromagnet. *Science* **351**, 587–590 (2016).
4. Takei, S., Yacoby, A., Halperin, B. I. & Tserkovnyak, Y. Spin superfluidity in the $\nu=0$ quantum Hall state of graphene. *Phys. Rev. Lett.* **116**, 216801 (2016).
5. Young, A. F. et al. Tunable symmetry breaking and helical edge transport in a graphene quantum spin Hall state. *Nature* **505**, 528–532 (2014).
6. Kharitonov, M. Edge excitations of the canted antiferromagnetic phase of the $\nu=0$ quantum Hall state in graphene: A simplified analysis. *Phys. Rev. B* **86**, 075450 (2012).
7. Takei, S., Moriyama, T., Ono, T. & Tserkovnyak, Y. Antiferromagnet-mediated spin transfer between a metal and a ferromagnet. *Phys. Rev. B* **92**, 020409 (2015).
8. Takei, S., Halperin, B. I., Yacoby, A. & Tserkovnyak, Y. Superfluid spin transport through antiferromagnetic insulators. *Phys. Rev. B* **90**, 094408 (2014).
9. Konig, J., Bonsager, M. C. & MacDonald, A. H. Dissipationless spin transport in thin film ferromagnets. *Phys. Rev. Lett.* **87**, 187202 (2001).
10. Qaiumzadeh, A., Skarsvåg, H., Holmqvist, C. & Brataas, A. Spin superfluidity in biaxial antiferromagnetic insulators. *Phys. Rev. Lett.* **118**, 137201 (2017).
11. Tsoi, M. et al. Generation and detection of phase-coherent current-driven magnons in magnetic multilayers. *Nature* **406**, 46–48 (2000).

12. Chumak, A. V., Vasyuchka, V. I., Serga, A. A. & Hillebrands, B. Magnon spintronics. *Nat. Phys.* **11**, 453–461 (2015).
13. Núñez, A. S., Duine, R. A., Haney, P. & MacDonald, A. H. Theory of spin torques and giant magnetoresistance in antiferromagnetic metals. *Phys. Rev. B* **73**, 214426 (2006).
14. Wang, H. L., Du, C. H., Hammel, P. C. & Yang, F. Y. Antiferromagnonic spin transport from $Y_3Fe_5O_{12}$ into NiO. *Phys. Rev. Lett.* **113**, 097202 (2014).
15. Hahn, C. et al. Conduction of spin currents through insulating antiferromagnetic oxides. *Europhys. Lett.* **108**, 57005 (2014).
16. Moriyama, T. et al. Anti-damping spin transfer torque through epitaxial nickel oxide. *Appl. Phys. Lett.* **106**, 162406 (2015).
17. Wang, H. L., Du, C. H., Hammel, P. C. & Yang, F. Y. Spin transport in antiferromagnetic insulators mediated by magnetic correlations. *Phys. Rev. B* **91**, 220410 (2015).
18. Nomura, K. & MacDonald, A. H. Quantum Hall ferromagnetism in graphene. *Phys. Rev. Lett.* **96**, 256602 (2006).
19. Alicea, J. & Fisher, M. P. A. Graphene integer quantum Hall effect in the ferromagnetic and paramagnetic regimes. *Phys. Rev. B* **74**, 075422 (2006).
20. Abanin, D. A. et al. Dissipative quantum Hall effect in graphene near the Dirac point. *Phys. Rev. Lett.* **98**, 196806 (2007).
21. Goerbig, M. O., Moessner, R. & Doucot, B. Electron interactions in graphene in a strong magnetic field. *Phys. Rev. B* **74**, 161407 (2006).
22. Kim, S., Lee, K. & Tutuc, E. Spin-polarized to valley-polarized transition in graphene bilayers at ν=0 in high magnetic fields. *Phys. Rev. Lett.* **107**, 016803 (2009).
23. Jiang, Z., Zhang, Y., Stormer, H. L. & Kim, P. Quantum Hall states near the charge-neutral Dirac point in graphene. *Phys. Rev. Lett.* **99**, 106802 (2007).
24. Checkelsky, J. G., Li, L. & Ong, N. P. Zero-energy state in graphene in a high magnetic field. *Phys. Rev. Lett.* **100**, 206801 (2008).
25. Checkelsky, J. G., Li, L. & Ong, N. P. Divergent resistance at the Dirac point in graphene: Evidence for a transition in a high magnetic field. *Phys. Rev. B* **79**, 115434 (2009).
26. Giesbers, A. J. M. et al. Gap opening in the zeroth Landau level of graphene. *Phys. Rev. B* **80**, 201403 (2009).
27. Zhao, Y., Cadden-Zimansky, P., Jiang, Z. & Kim, P. Symmetry breaking in the zero-energy Landau level in bilayer graphene. *Phys. Rev. Lett.* **104**, 066801 (2010).
28. Young, A. F. et al. Spin and valley quantum Hall ferromagnetism in graphene. *Nat. Phys.* **8**, 550–556 (2012).
29. Zhang, Y. et al. Landau-level splitting in graphene in high magnetic fields. *Phys. Rev. Lett.* **96**, 136806 (2006).
30. Sun, Q.-f & Xie, X. C. Spin-polarized ν=0 state of graphene: A spin superconductor. *Phys. Rev. B* **87**, 245427 (2013).
31. Abanin, D. A., Lee, P. A. & Levitov, L. S. Spin-filtered edge states and quantum Hall effect in graphene. *Phys. Rev. Lett.* **96**, 176803 (2006).
32. Takei, S. & Tserkovnyak, Y. Superfluid spin transport through easy-plane ferromagnetic insulators. *Phys. Rev. Lett.* **112**, 227201 (2014).
33. Wu, F., Sodemann, I., Araki, Y., MacDonald, A. H. & Jolicoeur, T. SO(5) symmetry in the quantum Hall effect in graphene. *Phys. Rev. B* **90**, 235432 (2014).
34. Chklovskii, D. B., Shklovskii, B. I. & Glazman, L. I. Electrostatics of edge channels. *Phys. Rev. B* **46**, 4026–4034 (1992).
35. Abanin, D. A. et al. Giant nonlocality near the Dirac point in graphene. *Science* **332**, 328–330 (2011).
36. Studer, M. & Folk, J. A. Origins of nonlocality near the neutrality point in graphene. *Phys. Rev. Lett.* **112**, 116601 (2014).
37. Chen, H., Kent, A. D., MacDonald, A. H. & Sodemann, I. Nonlocal transport mediated by spin supercurrents. *Phys. Rev. B* **90**, 220401 (2014).
38. Zhao, Y. et al. Experimental investigation of temperature-dependent Gilbert damping in permalloy thin films. *Sci. Rep.* **6**, 22890 (2016).
39. Johansen, Ø. & Linder, J. Current driven spin–orbit torque oscillator: ferromagnetic and antiferromagnetic coupling. *Sci. Rep.* **6**, 33845 (2016).
40. Kim, T. H., Grünberg, P., Han, S. H. & Cho, B. Ultrafast spin dynamics and switching via spin transfer torque in antiferromagnets with weak ferromagnetism. *Sci. Rep.* **6**, 35077 (2016).
41. Yankowitz, M. et al. Emergence of superlattice Dirac points in graphene on hexagonal boron nitride. *Nat. Phys.* **8**, 382–386 (2012).
42. Ozyilmaz, B. et al. Electronic transport and quantum Hall effect in bipolar graphene *p–n–p* junctions. *Phys. Rev. Lett.* **99**, 166804 (2007).
43. Wei, D. S. et al. Electrical generation and detection of spin waves in a quantum Hall ferromagnet. Preprint at https://arXiv.org/abs/1801.08534 (2018).

Acknowledgements

We thank H. Chen for helpful discussions. The work is supported by SHINES, which is an Energy Frontier Research Center funded by the Department of Energy (DOE) Basic Energy Sciences (BES) under Award #SC0012670. S.C. is supported by DOE BES under award ER 46940-DE-SC0010597 to study the quantum Hall effect in graphene. A.H.M. acknowledges partial support by the Welch Foundation under grant TBF1473. Part of this work was performed at the NHMFL, which is supported by NSF/DMR-0654118, the State of Florida, and the DOE. Growth of hBN crystals was supported by the Elemental Strategy Initiative conducted by the MEXT, Japan and a Grant-in-Aid for Scientific Research on Innovative Areas 'Science of Atomic Layers' from the Japan Society for the Promotion of Science (JSPS).

Author contribution

Y.B., A.H.M. and C.N.L. conceived the experiment. P.S., S.C. and D.Sh fabricated samples. K.T. and G.V. assisted with sample fabrication. P.S., J.Y., S.C., R.C. and D.Sm performed measurements. K.W. and T.T. provided materials. Y.B., P.S., A.H.M., M.B., R.L. and C.N.L. analysed and interpreted the data. P.S., Y.B., A.H.M., R.L. and C.N.L. wrote the manuscript. All authors discussed and commented on the manuscript.

Additional information

Supplementary information is available for this paper at https://doi.org/10.1038/s41567-018-0161-5.

Reprints and permissions information is available at www.nature.com/reprints.

Correspondence and requests for materials should be addressed to R.K.L. or Y.B. or A.H.M. or C.N.L.

Methods

Device Fabrication. The devices are fabricated from mechanically exfoliated monolayer graphene and few-layer hBN layers on SiO_2/Si wafers. We use a dry-transfer technique[44], during which a top-hBN layer attached to a polypropylene carbonate (PPC) sacrificial layer is used to pick up a graphene sheet. The graphene–hBN stack is then placed on top of the bottom-hBN layer and the stage is subsequently heated up to 90°C, when the PPC layer melts and the stack is released onto the surface of silicon wafer.

The next step of the fabrication process consists of defining the shape of the final sample. We use lithography and reactive ion etching by SF_6 plasma to define the multi-terminal geometry. A typical sample has 12 leads, 3 top gates and 1 back gate for proper characterization and measurement set-up. We subsequently couple the graphene sheet to one-dimensional Cr/Au (10/50 nm) metallic contacts. At the last step, Cr/Au metal top gates are deposited. Since each gate can be independently modulated, up to four different carrier densities can be created within the device. Moreover, every region is attached to one to two pairs of electrical leads, to enable its independent electrical characterization.

Device Characterization. Devices are characterized by transport measurements in helium-3 refrigerators. Typical measurements are outlined below.

1. Four terminal longitudinal resistivity R_{xx} is measured as a function of magnetic field B and back gate voltage (with top gates grounded) to characterize the robustness of quantum Hall states. This measurement is performed with standard lock-in techniques, using an a.c. excitation current of 50 nA at a frequency of 97 Hz. A typical data set $R_{xx}(V_{bg}, B)$ is shown in Supplementary Fig. 1a.
2. R_{xx} is measured at a constant magnetic field B as a function of the back (Supplementary Fig. 1b).
3. Two-terminal conductivity of the regions under the side top gates is measured as a function of back gate and side top gate at constant B, using an a.c. excitation voltage of 50 μV.
4. Non-local measurements with configurations described in the main text are performed using a d.c. voltage bias. The non-local signal is measured using a Stanford Research voltage amplifier SR560.

Data Availability. The data that support the findings of this study are available from the corresponding authors upon reasonable request.

References

44. Wang, L. et al. One-dimensional electrical contact to a two-dimensional material. *Science* **342**, 614–617 (2013).